

Quantum Valley Hall effect without Berry curvature

Rasoul Ghadimi,* Chiranjit Mondal,* Sunje Kim, and Bohm-Jung Yang[†]

Department of Physics and Astronomy, Seoul National University, Seoul 08826, Korea

Center for Theoretical Physics (CTP), Seoul National University, Seoul 08826, Korea and

Institute of Applied Physics, Seoul National University, Seoul 08826, Korea

(Dated: March 25, 2024)

The quantum valley Hall effect (QVHE) is characterized by the valley Chern number (VCN) in a way that one-dimensional (1D) chiral metallic states are guaranteed to appear at the domain walls (DW) between two domains with opposite VCN for a given valley. Although in the case of QVHE, the total BC of the system is zero, the BC distributed locally around each valley makes the VCN well-defined as long as inter-valley scattering is negligible. Here, we propose a new type of valley-dependent topological phenomenon that occurs when the BC is strictly zero at each momentum. Such zero Berry curvature (ZBC) QVHE is characterized by the valley Euler number (VEN) which is computed by integrating the Euler curvature around a given valley in two-dimensional (2D) systems with space-time inversion symmetry. 1D helical metallic states can be topologically protected at the DW between two domains with the opposite VENs when the DW configuration preserves either the mirror symmetry with respect to the DW or the combination of the DW space-time inversion, and chiral symmetries. We establish the fundamental origin of ZBC-QVHE. Also, by combining tight-binding model study and first-principles calculations, we propose stacked hexagonal bilayer lattices including h-BX ($X=As, P$) and large-angle twisted bilayer graphenes as candidate systems with robust helical DW states protected by VEN.

Introduction.— Quantum valley Hall effect (QVHE) is a topological phenomenon arising from nonzero Berry curvature (BC) around two valleys in time-reversal \mathcal{T} symmetric systems with broken inversion \mathcal{P} symmetry [1]. The valley Chern number (VCN) is defined as the integration of Berry curvature (BC) for a given valley, and its change over a domain counts the number of one-dimensional (1D) chiral metallic states at the domain wall (DW) [2–4]. Although the total BC of the system is zero due to \mathcal{T} -symmetry, if the BC is well-localized near each valley and the intervalley scattering is negligible, QVHE is robust. Bernal-stacked bilayer graphene is a representative system that exhibits QVHE under vertical electric field breaking \mathcal{P} symmetry [5–17]. Many interesting ideas have been proposed to realize QVHE not only in solid state systems [18–20] but also in classical wave systems [21–26]. These QVHE setups have potential application for valleytronics [27, 28].

The BC is an essential ingredient in various topological phenomena including the QVHE [29–31]. However, the recent studies of symmetry-protected topological states have uncovered various intriguing topological states that exist even in the absence of the BC [32–43]. One notable example is the topological states in two-dimensional (2D) systems with space-time inversion (\mathcal{I}_{ST}) symmetry, which appears in the form of either the combination of \mathcal{T} and \mathcal{P} in the absence of spin-orbit coupling or the combination of \mathcal{T} and two-fold rotation about the z -axis normal to the 2D plane (C_{2z}), irrespective of the presence or absence of spin-orbit coupling [44]. Although \mathcal{I}_{ST} symmetry forces the BC to vanish at every momentum, two isolated bands in 2D \mathcal{I}_{ST} symmetric systems can be characterized by an integer Euler number χ [45], which induces various intriguing physical properties [46]. For instance, two bands with an Euler number χ always possess 2χ number of Dirac points between them [45]. Moreover, a topological phase transition changing the Euler number accompanies pair-creation and pair-annihilation of nodal points

[45] which can be characterized by non-Abelian braiding processes [46–54]. Also, the Euler number is a fragile topological index characterizing the band topology of nearly flat bands in twisted bilayer graphene [45, 55–57], which reduces to a Z_2 second Stiefel-Whitney number when additional bands are included [44]. However, contrary to the case of stable topological states, the topological Euler bands cannot host boundary in-gap modes unless additional symmetries are imposed to the system [58], as is common in crystalline topological states [59].

In this work, we propose a new type of valley-dependent topological phenomenon appearing in the absence of the BC, dubbed a zero Berry curvature (ZBC) QVHE. The ZBC-QVHE is protected by the change of valley Euler number (VEN), similar to the conventional QVHE where the VCN changes over the domain wall. A nonzero change of VEN can protect one-dimensional (1D) helical metallic states along the DW between two domains when the DW configuration (DWC) satisfies either a mirror symmetry about the DW or C_{2z} together with a chiral symmetry. Here, the DWC indicates the structure composed of two domains having the opposite VEN with a DW in between. As a simple model to realize the ZBC-QVHE, we propose 2D bilayer structures such that each layer hosts QVHE in layer decoupled limit and the VCNs of the upper and lower layers have the opposite sign, thus the total system has zero BC at every momentum and no QVHE is expected.

Model.— To illustrate the idea, let us consider the AA'-stacked bilayer honeycomb lattice shown in Fig. 1(a) with the nearest-neighbor hopping within each layer as well as between layers, and a staggered sublattice potential. The low energy Hamiltonian at a valley (either K or K' as shown in Fig. 1(a)) can be written as

$$H_{\eta}(k_x, k_y) = v_{\eta}k_x\sigma_x\tau_0 + vk_y\sigma_y\tau_0 + m\sigma_z\tau_z + t_{\perp}\sigma_0\tau_x, \quad (1)$$

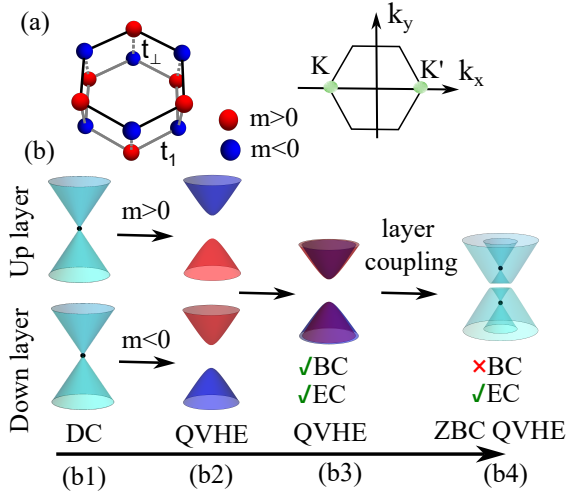


FIG. 1. (a) Lattice structure of the AA'-stacked honeycomb bilayers and the relevant Brillouin zone with two valleys at K and K' . (b) Schematic band structure evolution for zero Berry curvature quantum valley Hall effect (ZBC-QVHE). (b1, b2) Two degenerate Dirac cones (DCs) are gapped out by oppositely signed masses, which gives oppositely signed Berry curvature (BC) (represented by blue and red colors, respectively) for the occupied bands. (b3) Simple superposition of two decoupled gapped Dirac cones. (b4) Coupling of two gapped Dirac cones, respecting space-time inversion symmetry. The BC vanishes but the Euler curvature (EC) is well-defined and nonzero.

where $v = \frac{2}{3}t_1$ is the Fermi velocity, m is the staggered sublattice potential, and t_1, t_\perp are the nearest neighbor intralayer and interlayer coupling, respectively. $\eta = 1, -1$ indicates K and K' valleys, respectively. σ_i and τ_i ($i = x, y, z$) are the Pauli matrices for the sublattice and layer degrees of freedom, respectively, and σ_0 and τ_0 are corresponding 2×2 identity matrices.

We note that both \mathcal{P} and \mathcal{T} are symmetries of the full system but the Hamiltonian H_η for each valley is invariant only under their combination $\mathcal{PT} \equiv \mathcal{I}_{\text{ST}}$, dubbed the space-time inversion symmetry, which can be represented by $\mathcal{I}_{\text{ST}} = \sigma_x \tau_x K$ with complex conjugation operator K because \mathcal{P} interchanges the layers and sublattices. We note that m is the only mass term allowed under \mathcal{I}_{ST} . When $m = 0$, H_η is invariant under two mirrors $M_y : y \rightarrow -y$ and $M_z : z \rightarrow -z$ represented by $M_y = \sigma_x$ and $M_z = \tau_x$, as well as two chiral symmetries $\Pi_0 = \sigma_z \tau_z$ and $\Pi = \sigma_z \tau_y$. Here Π_0 is the bipartite chiral symmetry interchanging sublattices in the bilayer while $\Pi \propto M_z \Pi_0$. On the other hand, when $m \neq 0$, $\{\Pi, H_\eta\} = 0$ still holds while M_y, M_z, Π_0 symmetries are all broken.

Fig. 1(b) describes the band structure evolution of H_η around a valley. When $m = t_\perp = 0$, two degenerate Dirac cones, one from the top and the other from the bottom layers, appear at the Fermi energy ($E_F = 0$) [see Fig. 1(b1)]. Turning on nonzero m generates oppositely signed masses at two Dirac cones, which results in opposite Berry curvature between them [see Fig. 1(b2)]. Nonzero t_\perp couples two

gapped Dirac cones, which makes the BC vanishing at every momentum [see Fig. 1(b3, b4)]. However, both the upper and lower bands carry a half-integral Euler number, leading to ZBC-QVHE. Note that the presence of a single Dirac point in both the upper and lower bands (the blue dots in Fig. 1(b4)) is also consistent with their half-integral Euler number [47].

Topological invariant.— When interlayer coupling is neglected with $t_\perp = 0$, each layer carries a quantized VCN with the opposite sign between two layers. Explicitly, the valley Chern number $C_{\tau,\eta}$ for the valley η in the layer τ is $C_{\tau,\eta} = \frac{1}{2} \text{sgn}(m\eta\tau)$ where $\tau = +1, -1$ indicate the top and bottom layers, respectively. The change of VCN for each layer (and valley) over the domain wall $\Delta C_{\tau,\eta}^v \equiv 2C_{\tau,\eta} = \text{sgn}(m\eta\tau)$ supports gapless DW modes between two domains for the given valley. Since the VCNs of two decoupled layers have the opposite signs, the DW of the bilayer shown in Fig. 2(a) hosts two anti-propagating (helical) in-gap states per valley. The existence of these helical in-gap states at the DW is nothing but the manifestation of the QVHE in each layer [2, 7–16]. Interestingly, the helical DW modes survive even when $t_\perp \neq 0$ and thus the total VCN vanishes. Below, we show that the helical DW states are protected by the valley Euler number (VEN) of the bilayer.

In \mathcal{I}_{ST} -symmetric systems, one can always find a basis such that both the Hamiltonian and wave functions becomes real [32, 45, 46]. In two-dimensions, two real bands $|u^1(\mathbf{k})\rangle$ and $|u^2(\mathbf{k})\rangle$ can have an integer topological invariant, called the Euler number, defined as

$$\chi = \frac{1}{2\pi} \int_{BZ} \text{Ec}(\mathbf{k}) dk_x dk_y, \quad (2)$$

where $\text{Ec}(\mathbf{k}) = \langle \nabla u^1(\mathbf{k}) | \times | \nabla u^2(\mathbf{k}) \rangle$ is the Euler curvature and BZ indicates the two-dimensional Brillouin zone [45]. We note that the above integral can also be performed on a disk \mathcal{D} which is equal to the patch Euler number if we neglect 1D integration along the boarder of \mathcal{D} [46, 47]. We choose the size of \mathcal{D} large enough to suppress the Euler curvature along the boundary, then the half-integer value of $\chi_{\mathcal{D}}$ can be determined by integrating the Euler curvature, similar to the valley Chern number calculation by integrating the BC around a valley. For the coupled bilayer Hamiltonian in Eq. (1), the valley Euler number for a valley becomes $\chi_\eta = \frac{1}{2} \text{sgn}(m\eta)$, and the change of VEN over a DW is $\Delta \chi_\eta^v \equiv 2\chi_\eta = \text{sgn}(m\eta)$. The DW between two domains with opposite VENs can host helical DW states when the system satisfies certain symmetry conditions, as discussed below.

Note that by superposing two real bases, one can define the Chern bases $|\psi^\pm(\mathbf{k})\rangle \equiv (|u^1(\mathbf{k})\rangle \pm i|u^2(\mathbf{k})\rangle)/\sqrt{2}$ such that the Chern number of $|\psi^+(\mathbf{k})\rangle$ ($|\psi^-(\mathbf{k})\rangle$) is equal (opposite) to the Euler number of real bases [46, 60]. When two layers are decoupled with $t_\perp = 0$, the Chern bases are eigenstates of the Hamiltonian, which give the VCN of each layer. On the other hand, when $t_\perp \neq 0$, the Chern bases are not eigenstates anymore, and thus only the VEN is well-defined.

The relation between VCN and VEN is similar to that

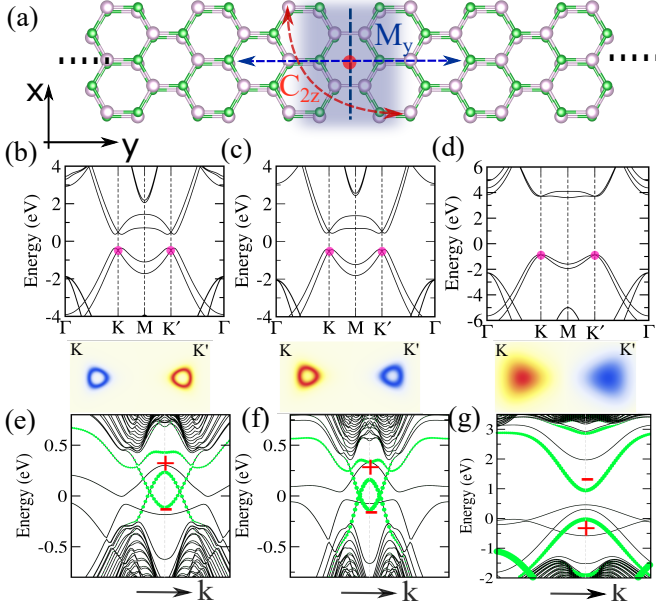


FIG. 2. Realization of ZBC-QVHE in AA' stacked bilayer h-BX ($X = \text{As, P, N}$). (a) Domain wall configuration (DWC) with M_y and C_{2z} symmetries. The blue dashed line and red disc represent the $M_y : y \rightarrow -y$ mirror and C_{2z} rotation centre respectively. (b,c,d) Bulk band structure (top) and Euler curvature distribution (bottom) for (b) h-BAs, (c) h-BP, and (d) h-BN. \mathcal{PT} symmetry-protected Dirac cones below the E_F are indicated by the purple dots at K and K' . (e,f,g) DW modes (green lines) for h-BAs, h-BP, and h-BN, respectively, where \pm indicate M_y mirror eigenvalues. As the bulk band gap and on-site potential change at the DW increase from (b) to (d), the Euler curvature spreads wider and the helical DW state pair gets closer and pair-annihilate.

between the Chern number and Z_2 invariant in quantum spin Hall systems. When two spin channels with the opposite Chern numbers are superposed, the Chern number of each spin channel is ill-defined if the spin-orbit coupling is present [61–63] while their Chern number difference is well-defined modulo two when time-reversal symmetry exists [64, 65]. Similarly, in our case, the VCN of each layer is ill-defined when interlayer coupling presents, while the VEN is well-defined when \mathcal{I}_{ST} symmetry exists

Stability of helical DW states.— The helical DW states related to the VEN can be protected when the DWC satisfies either M_y symmetry or the combination of chiral symmetry Π and DW space-time inversion $\mathcal{I}'_{\text{ST}} \equiv C_{2z}\mathcal{T}$ (see Fig. 2(a)). Using the Hamiltonian in Eq. (1), the DWC can be constructed by taking $m \rightarrow m(y)$, where $\lim_{|y| \rightarrow \infty} m(y) = \text{sign}(y)m_0$ and $m_0 > 0$. Accordingly, the DW is located along the x -direction. The Hamiltonian for DWC can be obtained from Eq. (1) by substituting $k_y \rightarrow -i\partial_y$ as

$$H_{\eta}^{\text{DW}}(k_x, y) = v\eta k_x \sigma_x \tau_0 - iv\partial_y \sigma_y \tau_0 + m(y) \sigma_z \tau_z + t_{\perp} \sigma_0 \tau_x. \quad (3)$$

In the following, we show how $M_y = \sigma_x$ symmetry can protect the helical DW states. When the DWC satisfies M_y ,

the DW becomes a M_y -invariant 1D space. Moreover, since M_y changes the sign of m in H_{η} , two domains related by M_y should have the opposite Euler number. Similarly, when interlayer coupling is neglected, two domains in each layer related by M_y should have the opposite Chern number.

For convenience, let us neglect interlayer coupling. Since each layer supports QVHE and the VCN of two layers have opposite signs, helical DW states should appear from each valley in the bilayer. The effective Hamiltonian for the helical DW states from one valley can be written as $H_0^{\text{DW}} = v'k_x \tau_z$ where τ_z gives a good quantum number when interlayer coupling is neglected. Since the DW is M_y invariant, each DW state should also carry a M_y eigenvalue. To have the M_y eigenvalue and the layer quantum number simultaneously, M_y should be represented by either $\tilde{M}_y = \tau_0$ or $\tilde{M}_y = \tau_z$ where the tilde symbol indicates the symmetry representation in the space spanned by helical DW states. $\tilde{M}_y = \tau_z$ prohibits the mass terms in the form of $H_m^{\text{DW}} = m_1\tau_x + m_2\tau_y$ even when interlayer coupling is turned on.

The representation $\tilde{M}_y = \tau_z$ in the DW can be confirmed as follows. For simplicity, let us consider $H^{\text{DW}}(y, \tau) = -iv\partial_y \sigma_y + \tau m \sigma_z$ corresponding to Eq. (3) with $k_x = 0$ and $t_{\perp} = 0$, where $\tau = \pm 1$ indicate the upper and lower layers, respectively. Because of the chiral symmetry $\{H^{\text{DW}}(y, \tau), \sigma_x\} = 0$, if $\psi(y)$ is a zero mode solution satisfying $H^{\text{DW}}(y, \tau)\psi(y) = 0$, $\sigma_x\psi(y)$ is also a zero mode solution. Since there is only one zero mode per layer, two solutions should be proportional to each other as $\sigma_x\psi(y) = \lambda\psi(y)$ where λ is a constant. Namely, $\psi(y)$ is an eigenstate of the chiral symmetry operator σ_x . Moreover, the mass term in $H^{\text{DW}}(y, \tau)$ has the opposite signs in two layers, the DW Hamiltonians for two layers are related as $\sigma_y H^{\text{DW}}(y, \tau = +1)\sigma_y = H^{\text{DW}}(y, \tau = -1)$. Thus, if $\psi(y)$ is a zero mode solution for one layer, $\sigma_y\psi(y)$ is the zero mode solution of the other layer. Since $\psi(y)$ and $\sigma_y\psi(y)$ have the opposite σ_x eigenvalues and $\psi(-y) = \psi(y)$, $\tilde{M}_y = \tau_z$ can be confirmed (see Supplemental Materials (SM) [66] for additional discussion). This symmetry representation is not affected by interlayer coupling if it is small enough to maintain the band gap. Therefore, the DWC with M_y symmetry can support helical DW states originating from VENs. Since the helical states have the opposite M_y eigenvalues, their crossing is stable.

The helical DW states can also be symmetry-protected when Π and $\mathcal{I}'_{\text{ST}} = C_{2z}\mathcal{T}$ satisfying $[\Pi, \mathcal{I}'_{\text{ST}}] = 0$ exist simultaneously. As noted above, Π is a combination of the bipartite chiral symmetry and M_z mirror. Also, if the DWC has C_{2z} symmetry, $\mathcal{I}'_{\text{ST}} = C_{2z}\mathcal{T}$ exists and takes the form of $\mathcal{I}'_{\text{ST}} = \sigma_x \mathcal{K}$ in Eq. (3). Since \mathcal{I}'_{ST} changes the sign of m in Eq. (1), two domains related by \mathcal{I}'_{ST} have the opposite VENs. Since C_{2z} does not mix layers, in the DW \mathcal{I}'_{ST} can be represented by $\tilde{\mathcal{I}}'_{\text{ST}} = K$ and forces $m_2 = 0$ in $H_m^{\text{DW}} = m_1\tau_x + m_2\tau_y$. The remaining mass $m_1\tau_x$ can be annihilated by imposing $\tilde{\Pi} = \tau_x$ that satisfies $[\tilde{\Pi}, \tilde{\mathcal{I}}'_{\text{ST}}] = 0$ [67–69].

Hexagonal bilayer materials.— As an example of AA'

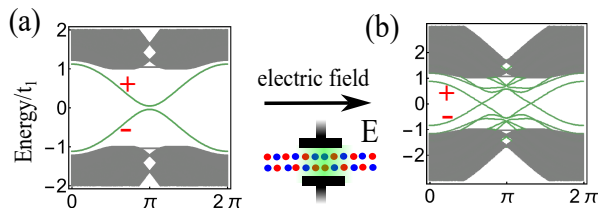


FIG. 3. The evolution of the helical DW dispersion under an external vertical electric field which can restore the helical DW states. DW dispersion (a) without and (b) with electric field.

stacked hexagonal bilayers, we consider h-BX (B=Boron and X= As, P, N) as shown in Fig. 2. Fig.2(a) describes the DWC with M_y and C_{2z} symmetries composed of two domains with opposite VENs. The band structures of h-BX single domains and the corresponding Euler curvature distribution around two valleys are shown in Fig.2(b,c,d) where we also identify the presence of a Dirac point between the two highest occupied bands at K and K' (purple dot in Fig.2(b,c,d)), respectively, demonstrating their half-integral valley Euler number [47]. Our DFT simulation (see SM for detail about the computation method) of the DWC confirms the existence of helical DW modes in h-BAs, and hBP as shown in Fig.2(e), and (f), respectively. Consistent with our prediction, the helical DW modes have opposite M_y eigenvalues.

In the case of h-BN, although the system respects all symmetry conditions to realize ZBC-QVHE, the helical DW modes are absent (see Fig.2 (g)). There are two reasons for this. One is because, as the band gap increases (see Fig. 2 (b,c,d)), the wavefunctions at K and K' are mixed more, which makes VEN ill-defined. To confirm it, we have computed the Euler curvature distribution near two valleys for these systems shown in the bottom panels of Fig. 2 (b,c,d). One can clearly see that the Euler curvature spreads wider as the band gap increases. In h-BN with the largest band gap, the helical DW states from two valleys are pair-annihilated, leading to the gapped DW modes (see Fig. 2 (g)).

The other reason is due to the abrupt change of the on-site potential at the DW, roughly proportional to the sublattice potential, occurring due to the atomic configuration change as shown in Fig. 2 (a). As h-BN with largest sublattice potential feels stronger potential variation at the DW, the helical DW modes from two valleys can be pair-annihilated. We note that as long as the DWC keeps the M_y mirror, the crossing of helical DW states from each valley is stable even if such potential variation happens. Interestingly, this on-site potential variation at the DW can be compensated by applying an external electric field to the domain. As shown in Fig. 3(a, b), the helical DW states can be recovered by applying an external electric field, which is obtained by using a tight-binding model relevant to h-BN with an additional out-of-plane electric field as described in detail in the SM.

Discussion.— We have proposed a new type of valley dependent topological phenomena, dubbed the ZBC-QVHE, induced by the VEN. Although the Euler number is a topolog-

ical invariant of two bands, the helical DW states are stable even in the presence of additional bulk bands as long as they do not disturb the half-integral Euler number of Euler bands at each valley. This is because the crossing between helical DW states from each valley is further protected by M_y symmetry of the DWC, which is well-defined even in multi-band systems. In the case of the helical DW states protected by \tilde{I}'_{ST} and $\tilde{\Pi}$ symmetries, the stability of the helical DW state crossing is guaranteed by the fact that H_{DW} has non-zero \mathcal{Z}_2 0-dimensional charge when commuting \tilde{I}'_{ST} and $\tilde{\Pi}$ symmetries are present [67].

In addition to h-BX materials, we have identified various candidate systems where ZBC-QVHE can be realized such as large-angle twisted bilayer graphene [29, 70–75], and hexagonal bilayer spin systems [76–81] as described in detail in SM.

Acknowledgements R.G. and C.M. thank Yuting Qian for fruitful discussions. R.G, C.M, S.K, and B-J.Y were supported by Samsung Science and Technology Foundation under Project Number SSTF-BA2002-06, the National Research Foundation of Korea (NRF) grant funded by the Korean government (MSIT) (No.2021R1A2C4002773, and No. NRF-2021R1A5A1032996).

* These authors contributed equally

† bjiang@snu.ac.kr

- [1] W. Yao, S. A. Yang, and Q. Niu, Edge states in graphene: From gapped flat-band to gapless chiral modes, *Phys. Rev. Lett.* **102**, 096801 (2009).
- [2] F. Zhang, A. H. MacDonald, and E. J. Mele, Valley chern numbers and boundary modes in gapped bilayer graphene, *Proceedings of the National Academy of Sciences* **110**, 10546 (2013), <https://www.pnas.org/doi/pdf/10.1073/pnas.1308853110>.
- [3] A. Vaezi, Y. Liang, D. H. Ngai, L. Yang, and E.-A. Kim, Topological edge states at a tilt boundary in gated multilayer graphene, *Phys. Rev. X* **3**, 021018 (2013).
- [4] J. Jung, F. Zhang, Z. Qiao, and A. H. MacDonald, Valley-hall kink and edge states in multilayer graphene, *Phys. Rev. B* **84**, 075418 (2011).
- [5] D. Xiao, W. Yao, and Q. Niu, Valley-contrasting physics in graphene: Magnetic moment and topological transport, *Phys. Rev. Lett.* **99**, 236809 (2007).
- [6] J. Liu, Z. Ma, J. Gao, and X. Dai, Quantum valley hall effect, orbital magnetism, and anomalous hall effect in twisted multilayer graphene systems, *Phys. Rev. X* **9**, 031021 (2019).
- [7] Y. Kim, K. Choi, J. Ihm, and H. Jin, Topological domain walls and quantum valley hall effects in silicene, *Phys. Rev. B* **89**, 085429 (2014).
- [8] I. Martin, Y. M. Blanter, and A. F. Morpurgo, Topological confinement in bilayer graphene, *Phys. Rev. Lett.* **100**, 036804 (2008).
- [9] G. W. Semenoff, V. Semenoff, and F. Zhou, Domain walls in gapped graphene, *Phys. Rev. Lett.* **101**, 087204 (2008).
- [10] Z. Qiao, J. Jung, Q. Niu, and A. H. MacDonald, Electronic highways in bilayer graphene, *Nano Letters* **11**, 3453 (2011), pMID: 21766817, <https://doi.org/10.1021/nl201941f>.
- [11] H. Pan, X. Li, F. Zhang, and S. A. Yang, Perfect valley filter in a topological domain wall, *Phys. Rev. B* **92**, 041404 (2015).

- [12] Z. Wang, S. Cheng, X. Liu, and H. Jiang, Topological kink states in graphene, *Nanotechnology* **32**, 402001 (2021).
- [13] T. Zhou, S. Cheng, M. Schleenvoigt, P. Schüffelgen, H. Jiang, Z. Yang, and I. Žutić, Quantum spin-valley hall kink states: From concept to materials design, *Phys. Rev. Lett.* **127**, 116402 (2021).
- [14] D. Ghader, Valley-polarized domain wall magnons in 2d ferromagnetic bilayers, *Scientific Reports* **10**, 16733 (2020).
- [15] M. Ezawa, Spin valleytronics in silicene: Quantum spin hall-quantum anomalous hall insulators and single-valley semimetals, *Phys. Rev. B* **87**, 155415 (2013).
- [16] M. Kim, Z. Jacob, and J. Rho, Recent advances in 2d, 3d and higher-order topological photonics, *Light: Science & Applications* **9**, 130 (2020).
- [17] W. Zhu, Y. Long, H. Chen, and J. Ren, Quantum valley hall effects and spin-valley locking in topological kane-mele circuit networks, *Phys. Rev. B* **99**, 115410 (2019).
- [18] L. Ju, Z. Shi, N. Nair, Y. Lv, C. Jin, J. Velasco, C. Ojeda-Aristizabal, H. A. Bechtel, M. C. Martin, A. Zettl, J. Analytis, and F. Wang, Topological valley transport at bilayer graphene domain walls, *Nature* **520**, 650 (2015).
- [19] J. Li, K. Wang, K. J. McFaul, Z. Zern, Y. Ren, K. Watanabe, T. Taniguchi, Z. Qiao, and J. Zhu, Gate-controlled topological conducting channels in bilayer graphene, *Nature Nanotechnology* **11**, 1060 (2016).
- [20] L.-J. Yin, H. Jiang, J.-B. Qiao, and L. He, Direct imaging of topological edge states at a bilayer graphene domain wall, *Nature Communications* **7**, 11760 (2016).
- [21] K. Qian, D. J. Apigo, C. Prodan, Y. Barlas, and E. Prodan, Topology of the valley-chern effect, *Phys. Rev. B* **98**, 155138 (2018).
- [22] J. Lu, C. Qiu, L. Ye, X. Fan, M. Ke, F. Zhang, and Z. Liu, Observation of topological valley transport of sound in sonic crystals, *Nature Physics* **13**, 369 (2017).
- [23] J.-W. Dong, X.-D. Chen, H. Zhu, Y. Wang, and X. Zhang, Valley photonic crystals for control of spin and topology, *Nature Materials* **16**, 298 (2017).
- [24] J. Noh, S. Huang, K. P. Chen, and M. C. Rechtsman, Observation of photonic topological valley hall edge states, *Phys. Rev. Lett.* **120**, 063902 (2018).
- [25] H. Li, Z. Wang, Z. Wang, C. Deng, J. Luo, J. Huang, X. Wang, and H. Yang, Acoustic multichannel transports of valley edge states in bilayer sonic crystals, *Applied Physics Letters* **121**, 243101 (2022), https://pubs.aip.org/aip/apl/article-pdf/doi/10.1063/5.0127559/16487480/243101.1_online.pdf.
- [26] J. Lu, C. Qiu, W. Deng, X. Huang, F. Li, F. Zhang, S. Chen, and Z. Liu, Valley topological phases in bilayer sonic crystals, *Phys. Rev. Lett.* **120**, 116802 (2018).
- [27] W. Yao, D. Xiao, and Q. Niu, Valley-dependent optoelectronics from inversion symmetry breaking, *Phys. Rev. B* **77**, 235406 (2008).
- [28] Z.-M. Yu, S. Guan, X.-L. Sheng, W. Gao, and S. A. Yang, Valley-layer coupling: A new design principle for valleytronics, *Phys. Rev. Lett.* **124**, 037701 (2020).
- [29] C. Mondal, R. Ghadimi, and B.-J. Yang, Quantum valley and subvalley hall effect in large-angle twisted bilayer graphene, *Phys. Rev. B* **108**, L121405 (2023).
- [30] C.-Z. Chang, C.-X. Liu, and A. H. MacDonald, Colloquium: Quantum anomalous hall effect, *Rev. Mod. Phys.* **95**, 011002 (2023).
- [31] K. Komatsu, Y. Morita, E. Watanabe, D. Tsuya, K. Watanabe, T. Taniguchi, and S. Moriyama, Observation of the quantum valley hall state in ballistic graphene superlattices, *Science Advances* **4**, eaaq0194 (2018), <https://www.science.org/doi/pdf/10.1126/sciadv.aaq0194>.
- [32] Y. X. Zhao and Y. Lu, *pt*-symmetric real dirac fermions and semimetals, *Phys. Rev. Lett.* **118**, 056401 (2017).
- [33] J. Ahn, D. Kim, Y. Kim, and B.-J. Yang, Band topology and linking structure of nodal line semimetals with Z_2 monopole charges, *Phys. Rev. Lett.* **121**, 106403 (2018).
- [34] J. Ahn and B.-J. Yang, Symmetry representation approach to topological invariants in $C_{2z}t$ -symmetric systems, *Phys. Rev. B* **99**, 235125 (2019).
- [35] F. N. Ünal, A. Bouhon, and R.-J. Slager, Topological euler class as a dynamical observable in optical lattices, *Phys. Rev. Lett.* **125**, 053601 (2020).
- [36] C. Chen, W. Wu, Z.-M. Yu, Z. Chen, Y. X. Zhao, X.-L. Sheng, and S. A. Yang, Graphyne as a second-order and real chern topological insulator in two dimensions, *Phys. Rev. B* **104**, 085205 (2021).
- [37] M. Ezawa, Topological euler insulators and their electric circuit realization, *Phys. Rev. B* **103**, 205303 (2021).
- [38] W. Zhao, Y.-B. Yang, Y. Jiang, Z. Mao, W. Guo, L. Qiu, G. Wang, L. Yao, L. He, Z. Zhou, Y. Xu, and L. Duan, Quantum simulation for topological euler insulators, *Communications Physics* **5**, 223 (2022).
- [39] R. Takahashi and T. Ozawa, Bulk-edge correspondence of stiefel-whitney and euler insulators through the entanglement spectrum and cutting procedure, *Phys. Rev. B* **108**, 075129 (2023).
- [40] B. Jiang, A. Bouhon, S.-Q. Wu, Z.-L. Kong, Z.-K. Lin, R.-J. Slager, and J.-H. Jiang, Experimental observation of meronic topological acoustic euler insulators (2022), arXiv:2205.03429 [cond-mat.mes-hall].
- [41] H. Lim, S. Kim, and B.-J. Yang, Real hopf insulator, *Phys. Rev. B* **108**, 125101 (2023).
- [42] S. Park, Y. Hwang, H. C. Choi, and B.-J. Yang, Topological acoustic triple point, *Nature Communications* **12**, 6781 (2021).
- [43] J. Kim, S. S. Baik, S. W. Jung, Y. Sohn, S. H. Ryu, H. J. Choi, B.-J. Yang, and K. S. Kim, Two-dimensional dirac fermions protected by space-time inversion symmetry in black phosphorus, *Phys. Rev. Lett.* **119**, 226801 (2017).
- [44] J. Ahn, S. Park, D. Kim, Y. Kim, and B.-J. Yang, Stiefel-whitney classes and topological phases in band theory, *Chinese Physics B* **28**, 117101 (2019).
- [45] J. Ahn, S. Park, and B.-J. Yang, Failure of nielsen-ninomiya theorem and fragile topology in two-dimensional systems with space-time inversion symmetry: Application to twisted bilayer graphene at magic angle, *Phys. Rev. X* **9**, 021013 (2019).
- [46] A. Bouhon, Q. Wu, R.-J. Slager, H. Weng, O. V. Yazyev, and T. Bzdušek, Non-abelian reciprocal braiding of weyl points and its manifestation in zrte, *Nature Physics* **16**, 1137 (2020).
- [47] B. Peng, A. Bouhon, B. Monserrat, and R.-J. Slager, Phonons as a platform for non-abelian braiding and its manifestation in layered silicates, *Nature Communications* **13**, 423 (2022).
- [48] B. Peng, A. Bouhon, R.-J. Slager, and B. Monserrat, Multigap topology and non-abelian braiding of phonons from first principles, *Phys. Rev. B* **105**, 085115 (2022).
- [49] H. Qiu, Q. Zhang, T. Liu, X. Fan, F. Zhang, and C. Qiu, Minimal non-abelian nodal braiding in ideal metamaterials, *Nature Communications* **14**, 1261 (2023).
- [50] B. Jiang, A. Bouhon, Z.-K. Lin, X. Zhou, B. Hou, F. Li, R.-J. Slager, and J.-H. Jiang, Experimental observation of non-abelian topological acoustic semimetals and their phase transitions, *Nature Physics* **17**, 1239 (2021).
- [51] A. Bouhon, T. c. v. Bzdušek, and R.-J. Slager, Geometric approach to fragile topology beyond symmetry indicators, *Phys. Rev. B* **102**, 115135 (2020).

- [52] R.-J. Slager, A. Bouhon, and F. N. Únal, Floquet multi-gap topology: Non-abelian braiding and anomalous dirac string phase (2022), arXiv:2208.12824 [cond-mat.mes-hall].
- [53] T. Jiang, R.-Y. Zhang, Q. Guo, B. Yang, and C. T. Chan, Two-dimensional non-abelian topological insulators and the corresponding edge/corner states from an eigenvector frame rotation perspective, *Phys. Rev. B* **106**, 235428 (2022).
- [54] Q. Guo, T. Jiang, R.-Y. Zhang, L. Zhang, Z.-Q. Zhang, B. Yang, S. Zhang, and C. T. Chan, Experimental observation of non-abelian topological charges and edge states, *Nature* **594**, 195 (2021).
- [55] A. Bouhon, A. M. Black-Schaffer, and R.-J. Slager, Wilson loop approach to fragile topology of split elementary band representations and topological crystalline insulators with time-reversal symmetry, *Phys. Rev. B* **100**, 195135 (2019).
- [56] H. C. Po, L. Zou, T. Senthil, and A. Vishwanath, Faithful tight-binding models and fragile topology of magic-angle bilayer graphene, *Phys. Rev. B* **99**, 195455 (2019).
- [57] Z. Song, Z. Wang, W. Shi, G. Li, C. Fang, and B. A. Bernevig, All magic angles in twisted bilayer graphene are topological, *Phys. Rev. Lett.* **123**, 036401 (2019).
- [58] K. Wang, J.-X. Dai, L. B. Shao, S. A. Yang, and Y. X. Zhao, Boundary criticality of \mathcal{PT} -invariant topology and second-order nodal-line semimetals, *Phys. Rev. Lett.* **125**, 126403 (2020).
- [59] Y. Ando and L. Fu, Topological crystalline insulators and topological superconductors: From concepts to materials, *Annual Review of Condensed Matter Physics* **6**, 361 (2015), <https://doi.org/10.1146/annurev-conmatphys-031214-014501>.
- [60] Y. Guan, A. Bouhon, and O. V. Yazyev, Landau levels of the euler class topology, *Phys. Rev. Res.* **4**, 023188 (2022).
- [61] C. L. Kane and E. J. Mele, Quantum spin hall effect in graphene, *Phys. Rev. Lett.* **95**, 226801 (2005).
- [62] B. A. Bernevig and S.-C. Zhang, Quantum spin hall effect, *Phys. Rev. Lett.* **96**, 106802 (2006).
- [63] L. Sheng, D. N. Sheng, C. S. Ting, and F. D. M. Haldane, Nondissipative spin hall effect via quantized edge transport, *Phys. Rev. Lett.* **95**, 136602 (2005).
- [64] C. L. Kane and E. J. Mele, Z_2 topological order and the quantum spin hall effect, *Phys. Rev. Lett.* **95**, 146802 (2005).
- [65] L. Fu and C. L. Kane, Topological insulators with inversion symmetry, *Phys. Rev. B* **76**, 045302 (2007).
- [66] See the Supplemental Materials (SM) for details on tight binding, derivation of edge modes, ZBC QVHE in twisted bilayer graphene, ZBC QVHE in canted antiferromagnetic systems, and DFT computation [82–84].
- [67] T. c. v. Bzdušek and M. Sigrist, Robust doubly charged nodal lines and nodal surfaces in centrosymmetric systems, *Phys. Rev. B* **96**, 155105 (2017).
- [68] S. Kim, D.-C. Ryu, and B.-J. Yang, Linking structures of doubly charged nodal surfaces in centrosymmetric superconductors, *Phys. Rev. B* **103**, 224523 (2021).
- [69] C. Mondal, S. Kim, and B.-J. Yang, Unremovable linked nodal structures protected by crystalline symmetries in stacked bilayer graphene with kekulé texture, *Phys. Rev. B* **106**, L121118 (2022).
- [70] E. J. Mele, Interlayer coupling in rotationally faulted multilayer graphenes, *Journal of Physics D: Applied Physics* **45**, 154004 (2012).
- [71] S. Shallcross, S. Sharma, and O. A. Pankratov, Quantum interference at the twist boundary in graphene, *Phys. Rev. Lett.* **101**, 056803 (2008).
- [72] E. J. Mele, Commensuration and interlayer coherence in twisted bilayer graphene, *Phys. Rev. B* **81**, 161405 (2010).
- [73] M. Kindermann, Topological crystalline insulator phase in graphene multilayers, *Phys. Rev. Lett.* **114**, 226802 (2015).
- [74] M. J. Park, Y. Kim, G. Y. Cho, and S. Lee, Higher-order topological insulator in twisted bilayer graphene, *Phys. Rev. Lett.* **123**, 216803 (2019).
- [75] B.-B. Liu, X.-T. Zeng, C. Chen, Z. Chen, and X.-L. Sheng, Second-order and real chern topological insulator in twisted bilayer α -graphyne, *Phys. Rev. B* **106**, 035153 (2022).
- [76] S. Wang, P. Zhang, C. Ren, H. Tian, J. Pang, C. Song, and M. Sun, Valley hall effect and magnetic moment in magnetized silicene, *Journal of Superconductivity and Novel Magnetism* **32**, 2947 (2019).
- [77] S. F. Islam and C. Benjamin, A scheme to realize the quantum spin-valley hall effect in monolayer graphene, *Carbon* **110**, 304 (2016).
- [78] H. Yang, J. Xu, Z. Xiong, X. Lu, R.-Y. Zhang, H. Li, Y. Chen, and S. Zhang, Optically reconfigurable spin-valley hall effect of light in coupled nonlinear ring resonator lattice, *Phys. Rev. Lett.* **127**, 043904 (2021).
- [79] M. Ezawa, Monolayer topological insulators: Silicene, germanene, and stanene, *Journal of the Physical Society of Japan* **84**, 121003 (2015), <https://doi.org/10.7566/JPSJ.84.121003>.
- [80] X. Li, T. Cao, Q. Niu, J. Shi, and J. Feng, Coupling the valley degree of freedom to antiferromagnetic order, *Proceedings of the National Academy of Sciences* **110**, 3738 (2013), <https://www.pnas.org/doi/pdf/10.1073/pnas.1219420110>.
- [81] A. L. Rakhmanov, A. V. Rozhkov, A. O. Sboychakov, and F. Nori, Instabilities of the aa -stacked graphene bilayer, *Phys. Rev. Lett.* **109**, 206801 (2012).
- [82] P. E. Blöchl, Projector augmented-wave method, *Phys. Rev. B* **50**, 17953 (1994).
- [83] G. Kresse and J. Hafner, Ab initio molecular dynamics for liquid metals, *Phys. Rev. B* **47**, 558 (1993).
- [84] G. Kresse and D. Joubert, From ultrasoft pseudopotentials to the projector augmented-wave method, *Phys. Rev. B* **59**, 1758 (1999).

SUPPLEMENTAL MATERIAL: Quantum Valley Hall effect without Berry curvature

Rasoul Ghadimi, Chiranjit Mondal, Sunje Kim, and Bohm-Jung Yang
(Dated: March 25, 2024)

S1. TIGHT BINDING AND EDGE THEORY

The simple tight-binding Hamiltonian of AA'-stacked bilayer graphene can be read as [see Fig. S1(a, b)]

$$H = \sum_{\alpha, \alpha', l, l', i, j} (t_{i,j}^{\alpha, l; \alpha', l'} + m_{\alpha, l} \delta_{l, l'} \delta_{\alpha, \alpha'} \delta_{i, j}) |\alpha, l, i\rangle \langle \alpha', l', j|, \quad (\text{S.1})$$

where $|\alpha, l, i\rangle$, and $\langle \alpha, l, i|$ are ket and bra states of electron at given sublattice $\alpha = A, B$, layer $l = 1, 2$, and site i index. In Eq. (S.1) $t_{i,j}^{\alpha, l; \alpha', l'}$, and $m_{\alpha, l}$ indicate hopping energy and onsite potential of electrons. In the following, we consider t_1 , and t_2 as the nearest-neighbor and next-nearest-neighbor coupling inside each layer, while the vertical hopping is given by t_{\perp} . The staggered sublattice potential is considered as $m = m_{A,1} = -m_{B,1} = -m_{A,2} = m_{B,2}$, mimicking bilayer h-BX systems. By applying the Fourier transformation, $|\alpha, l, i\rangle = \sum_{\mathbf{k}} \exp(i\mathbf{k} \cdot \mathbf{r}_i) |\alpha, l, \mathbf{k}\rangle$, one can block diagonalize the Hamiltonian in the momentum space as $H = \sum_{\mathbf{k}, \alpha, \alpha', l, l'} H_{\alpha, l; \alpha', l'}(\mathbf{k}) |\alpha, l, \mathbf{k}\rangle \langle \alpha', l', \mathbf{k}|$, where $H(\mathbf{k})$ is a matrix given by

$$H(\mathbf{k}) = \epsilon(\mathbf{k})\sigma_0\tau_0 + h_x(\mathbf{k})\sigma_x\tau_0 + h_y(\mathbf{k})\sigma_y\tau_0 + m\sigma_z\tau_z + t_{\perp}\sigma_0\tau_x. \quad (\text{S.2})$$

σ_i and τ_i ($i = x, y, z$) represent the Pauli matrices for the sublattice and layer degrees of freedom, respectively, and σ_0 and τ_0 are corresponding 2×2 identity matrices. Here, $\epsilon(\mathbf{k})$, $h_x(\mathbf{k})$, and $h_y(\mathbf{k})$ are function of momenta and given explicitly as

$$\epsilon(\mathbf{k}) = 2t_2 \left(2 \cos\left(\frac{\sqrt{3}k_x}{2}\right) \cos\left(\frac{3k_y}{2}\right) + \cos\left(\sqrt{3}k_x\right) \right), \quad (\text{S.3})$$

$$h_x(\mathbf{k}) = t_1 \left(2 \cos\left(\frac{\sqrt{3}k_x}{2}\right) \cos\left(\frac{k_x}{2}\right) + \cos(k_y) \right), \quad (\text{S.4})$$

$$h_y(\mathbf{k}) = t_1 \left(\sin(k_y) - 2 \cos\left(\frac{\sqrt{3}k_x}{2}\right) \sin\left(\frac{k_y}{2}\right) \right). \quad (\text{S.5})$$

In the absence of m, t_{\perp} , Eq. (S.2) results in two degenerated Dirac cones at each valley $\eta = \pm 1$, located at $K_{\eta} = \eta(\frac{4\pi}{3\sqrt{3}}, 0)$. It is clear from Fig. S1(e), that the domain wall is \mathcal{M}_y symmetric. We plot the band structure for a ribbon that is periodic along the x-direction as shown in Fig. S1(f). The mirror eigenvalue $+1$ and -1 of each band in Fig. S1(f) are indicated by red and blue colors. We can see the helical states obtain opposite mirror eigenvalues, and therefore their crossing is stable. To prove this analytically, further, we derive domain wall states wave-function explicitly. To start we first obtain the low energy model of Eq. (S.2) by assuming small m and t_{\perp} at K_{η} a valley K_{η}

$$H = -3t_2\sigma_0\tau_0 + \frac{3}{2}k_x\eta t_1\sigma_x\tau_0 + \frac{3}{2}k_y t_1\sigma_y\tau_0 + m\sigma_z\tau_z + t_{\perp}\sigma_0\tau_x. \quad (\text{S.6})$$

Note that nonzero t_2 only trivially shifts energy dispersion along the energy axis and therefore in the following discussion we set $t_2 = 0$. The domain is constructed by assuming $m \rightarrow m(y)$, where $\lim_{|y| \rightarrow \infty} m(y) = \text{sign}(y)m_0$. Accordingly, the domain is located along the x direction. The domain wall wave function is obtained by substituting $k_y \rightarrow -i\partial_y$. To proceed we furthermore assume $k_x = 0, t_{\perp} = 0$ and later treat them perturbatively. Therefore we need to solve

$$-i\frac{3}{2}t_1\sigma_y\tau_0\partial_y |\psi(y)\rangle + m(y)\sigma_z\tau_z |\psi(y)\rangle = 0 \quad (\text{S.7})$$

where $|\psi(y)\rangle$ is a spinor wave function that depends on y and we assume that at $k_x = 0$, the energy of domain modes is zero (see Fig. S1(f) that crossing is located at Dirac points). To solve this equation we can express $|\psi(y)\rangle$ in a way that Eq. S.7 convert to a non-spinor equation. This equation can be more simplified if we express it as $|\psi(y)\rangle = \sigma_z |\psi'(y)\rangle$,

$$\frac{3}{2}t_1\sigma_x\tau_0\partial_y |\psi'(y)\rangle + m(y)\tau_z |\psi'(y)\rangle = 0 \quad (\text{S.8})$$

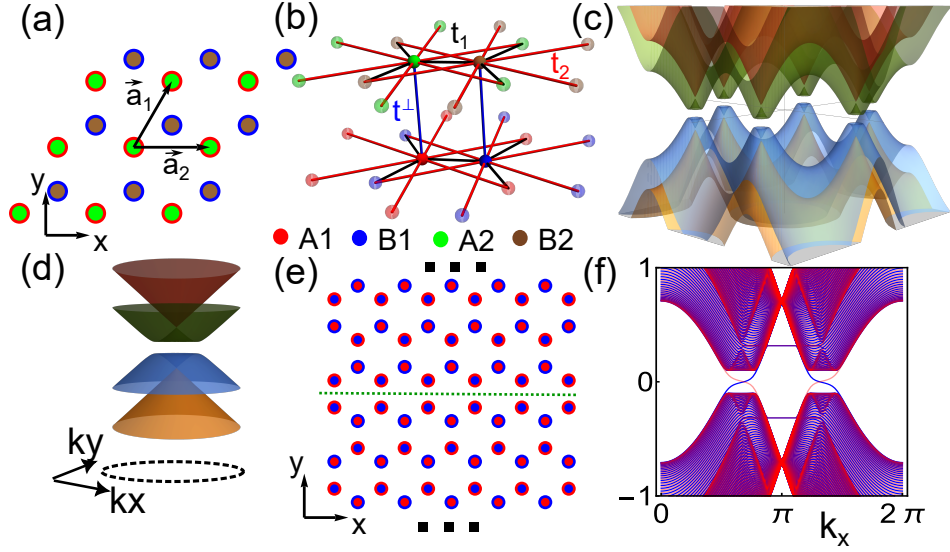


FIG. S1. (a, b) Lattice structure and hopping parameter of AA' stack of bilayer h-BX. (c) The energy dispersion of Eq. (S.1). (d) The magnified view of the (c) around a valley. The black dashed loop represents the boundary that we calculate the valley Euler number. (e) Domain wall structure, where the domain wall is represented by the dashed green line. The x direction is periodic. The red and blue disks show sites with opposite signs of onsite potential. (f) Energy dispersion of domain wall of (e) is plotted [we set $t_{\perp}/t_1 = 0.3$, $t_2 = 0$, and $m/t_1 = 0.1$]. The red and blue colors in (f) indicated the given band's mirror eigenvalues (± 1).

By applying τ_z on both sides of equation we arrived at

$$\frac{3}{2}t_1\sigma_x\tau_z\partial_y|\psi'(y)\rangle + m(y)|\psi'(y)\rangle = 0 \quad (\text{S.9})$$

It is obvious that the $|\psi'(y)\rangle$ should be eigenstate of τ_z and σ_x or equivalently $|\psi'(y)\rangle = f(y)|\tau_z = \tau, \sigma_x = \sigma\rangle$, where $\sigma = \pm 1$ and $\tau = \pm 1$. Here $f(y)$ is a y -dependent function that should be localized at the domain and can obtain by putting $|\psi'(y)\rangle$ in S.9,

$$\left(\frac{3}{2}t_1\sigma\tau\partial_y f(y) + m(y)f(y)\right)|\tau_z = \tau, \sigma_x = \sigma\rangle = 0. \quad (\text{S.10})$$

Therefore to satisfying Eq. S.10, $f(y)$ should solve

$$\frac{3}{2}t_1\sigma\tau\partial_y f(y) + m(y)f(y) = 0. \quad (\text{S.11})$$

Now solving this equation is very easy and we obtain

$$f(y) = f(y_0) \exp\left[-\sigma\tau \int_{y_0}^y \frac{2}{3t_1}m(y')dy'\right] \quad (\text{S.12})$$

Note that to describe the domain wall $f(y)$ should decay very fast to zero when $|y|$ increases. Note that $\lim_{|y|\rightarrow\infty} m(y) = \text{sign}(y)m_0$. Therefore for large $|y| \gg 0$, we can obtain $f(y)$ as

$$f(y) \propto \exp\left[-\frac{2}{3t_1}\sigma\tau\text{sign}(y)m_0y\right] \quad (\text{S.13})$$

or equivalently

$$f(y) \propto \exp\left[-\frac{2}{3t_1}\sigma\tau m_0|y|\right] \quad (\text{S.14})$$

It is easy to see that $f(|y| \gg 0) \rightarrow 0$ if $-\sigma\tau\frac{2m_0}{3t_1} < 0$ or equivalently $\sigma\tau = \text{sign}(t_1m_0)$. This means that σ and τ are not independent and therefore only two combinations of $\sigma = \pm 1$, $\tau = \pm 1$ can give localized domain wall states. Combining the previous calculation, the following ansatz gives a zero energy state at the domain wall

$$|\psi_{\text{Dw}}^{\tau}(y)\rangle \equiv \frac{1}{\mathcal{N}} e^{-\text{sign}(m_0) \int_0^y \frac{2}{3|t_1|} m(y') dy'} \sigma_z |\tau_z = \tau, \sigma_x = \text{sign}(\tau m_0 t_1)\rangle, \quad (\text{S.15})$$

where we introduce \mathcal{N} for normalization.

The mirror symmetry is given by $\mathcal{M}_y = \sigma_x(y \rightarrow -y)$. Note that two domain wall states have opposite eigenvalues of σ_x . Therefore $|\psi_{\text{DW}}^{\pm}(y)\rangle$ are eigenstates of mirror symmetry and have opposite mirror eigenvalues. Note that mirror symmetry keeps y dependent function invariant, which can be proven as follows

$$e^{-\text{sign}(m_0) \int_0^{-y} \frac{2}{3|t_1|} m(y') dy'} \underset{y' \rightarrow -y'}{=} e^{-\text{sign}(m_0) \int_0^y \frac{2}{3|t_1|} m(-y') d(-y')} \underset{m(-y') = -m(y')}{=} e^{-\text{sign}(m_0) \int_0^y \frac{2}{3|t_1|} m(y') d(y')}. \quad (\text{S.16})$$

To obtain domain wall Hamiltonian, we have to project other terms like $\frac{3}{2}k_x \eta t_1 \sigma_x \tau_0 + t_{\perp} \sigma_0 \tau_x$ into zero energy domain wall modes. The first term gives

$$H_{\text{DW}} \equiv \int_{-\infty}^{\infty} dy \langle \psi_{\text{DW}}^{\tau}(y) | \frac{3}{2} k_x \eta t_1 \sigma_x \tau_0 | \psi_{\text{DW}}^{\tau'}(y) \rangle \propto \frac{3}{2} |t_1| \text{sign}(\eta m_0) k_x (\tau_z)_{\tau, \tau'}.$$

But the second term $t_{\perp} \sigma_0 \tau_x$ changes τ while keeping σ intact. But as we saw before σ and τ are locked and therefore this term gives zero if we project it to the domain wall states, equivalently

$$\int_{-\infty}^{\infty} dy \langle \psi_{\text{DW}}^{\tau}(y) | t_{\perp} \sigma_0 \tau_x | \psi_{\text{DW}}^{\tau'}(y) \rangle = 0.$$

This means that the domain wall crossing is protected even after coupling two layers.

To calculate the valley Euler number, we first assume the sublattice potential m is small and then choose a patch around the Dirac point between two lower bands with a large radius to neglect the effect of m on the border of the patch. Then we fixed the wave function on the boundary of the patch (black lines in Fig. S1(d)) and found that the sign of the valley Euler number changes with the change of the sign of sublattice potential m .

S2. DFT COMPUTATIONAL DETAILS:

First principle calculations were carried out using projector augmented wave (PAW)[1] formalism based on Density Functional Theory (DFT) as implemented in the Vienna ab-initio Simulation Package (VASP).[2, 3] The generalized-gradient approximation by Perdew-Burke-Ernzerhof (PBE)[3] was employed to describe the exchange and correlation. An energy cut-off of 400 eV is used to truncate the plane-wave basis sets. DFT-D3 method has been applied for Van der Waals forces correction. We construct the domain of length around 180\AA with at least 15\AA vacuum size along the non-periodic directions to avoid any interactions between the periodic images. The Brillouin zone (BZ) for the 1D ribbon is integrated using $1 \times 5 \times 1$ Γ -centered k -mesh. We relax the bilayer systems and then use the optimized lattice constants and layer separation distances to construct the 1D ribbon systems for h-BX (X=N, P, and As). Due to the large size of the 1D ribbon, we only used the relaxed bulk parameters. To calculate the Euler curvature of the h-BX, we construct a tight-binding Hamiltonian for the compounds using p_z orbitals. With appropriate sublattice potential, we reproduce the band gap of the DFT results. Then we calculate the Euler curvature using the fitted Hamiltonian.

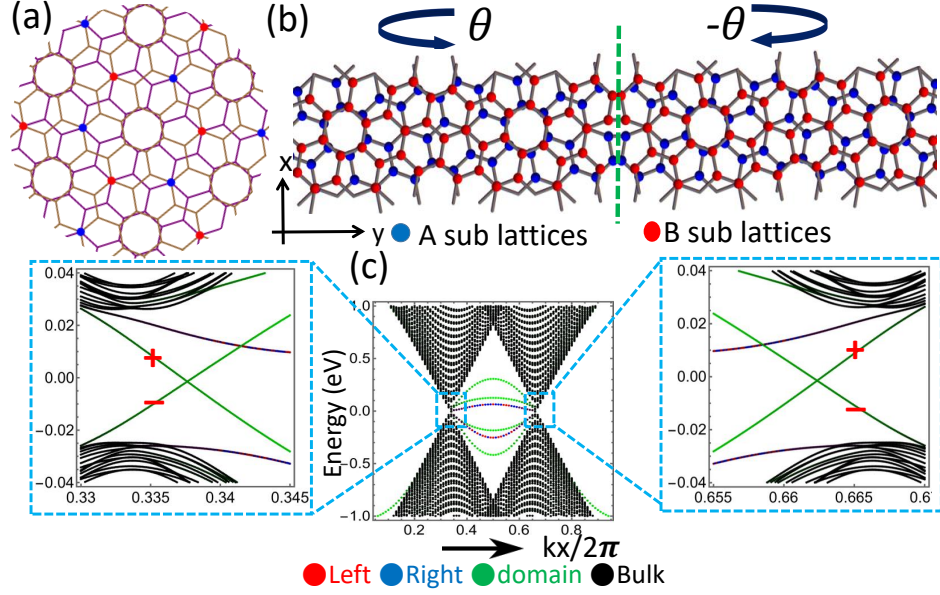


FIG. S2. Realization of the ZBC QVHE in Twisted Bilayer Graphene (TBG). (a) The SEE configuration of TBG at $\theta = 38.21$. (b) The domain wall modes of ZBC QVHE can be achieved by symmetrically attaching two SEE configurations with opposite rotation angles $+\theta$ and $-\theta$. (c) Energy dispersion of the domain wall and its magnified versions around two valleys (we only show a few eigenvalues near the energy gap). In Plots, the red plus and minus indicate opposite mirror eigenvalues for the given domain modes wave functions.

S3. TWISTED BILAYER GRAPHENE

In Ref. 4, we investigated the QVHE in a large-angle TBG in its sublattice odd configuration [5, 6]. In the presence of a perpendicular electric field, this configuration acquires a non-zero valley Chern number and shows the QVHE. However, the energy band dispersion of the sublattice even (SEE) configuration is the same as AA graphene but nodal lines are gapped out. The SEE configuration possesses \mathcal{I}_{ST} as the combination of two-fold rotation and time reversal symmetry i.e., $\mathcal{C}_{2z}\mathcal{T}$ (Fig. S2(a)) which leads to the absence of valley Chern number. It has been shown that the SEE configuration has a nontrivial Stiefel Whitney index, exhibiting corner modes [7]. Therefore, two occupied bands around the Fermi energy host non-trivial Euler class.

The Hamiltonian of SEE configuration was derived by Mele in Ref.[8] and is given by [9]

$$H = \nu(k_x\eta\sigma_x + k_y\sigma_y) + \gamma e^{i\phi\eta\tau_z\sigma_z}\tau_x e^{-i\phi\eta\tau_z\sigma_z}, \quad (\text{S.17})$$

where σ , τ , and η are defined as sublattice, layer and valley degree of freedom. Here γ and ϕ are the parameters which depend on the rotation angle. Here $\mathcal{C}_{2z}\mathcal{T} = \sigma_x K$. This Hamiltonian can be represented by

$$H = \nu(k_x\eta\sigma_x + k_y\sigma_y) + \gamma \cos 2\phi\tau_x - \eta\gamma \sin 2\phi\tau_y\sigma_z. \quad (\text{S.18})$$

By transferring basis using a unitary matrix $U = e^{i\pi/4\tau_x}$ we obtain

$$U^\dagger H U = \nu(\eta k_x\sigma_x + k_y\sigma_y) + \gamma \cos 2\phi\tau_x + \eta\gamma \sin 2\phi\sigma_z\tau_z \quad (\text{S.19})$$

which is same as the Hamiltonian for ZBC QVHE in the main text (Eq. (1)), where mass and inter-layer coupling are replaced by $\eta\gamma \sin 2\phi$, and $\gamma \cos 2\phi$, respectively. Therefore, changing the sign of ϕ changes the valley Euler number. Therefore the sign of the gap can be determined by the sign of ϕ . As we can see easily from Eq. S.17, we can flip the sign of ϕ by $\tau_x H \tau_x$. Such operation is equivalent to the changing of layers, which is equivalent to twisting with the opposite angle. Furthermore sign of ϕ can be exchange using a mirror operator $\mathcal{M} = \sigma_x(k_y \rightarrow -k_y)$. Also the sign of the ϕ can be exchange using a \mathcal{PT} operation, $\mathcal{PT} = \sigma_x\tau_x K$.

To achieve the boundary modes related to ZBC QVHE, we designed a setup, that involves the joining of two twisted bilayers with opposite commensurate twisting angles and preparing the interface to respect the domain wall mirror symmetry (and/or domain wall space-time symmetry $\mathcal{I}'_{ST} = \mathcal{PT}$) as shown in Fig. S2(b). We found that the energy dispersion of the system shows gapless helical states for each valley and it unequivocally confirms the ZBC QVHE in the SEE configuration of large-angle TBG (see Fig. S2(c)). Furthermore, we anticipate the existence of such a ZBC QVHE in various other twisted bilayer systems,

including α -graphyne as α -graphyne possess exactly similar band dispersion and contain the same symmetries [10]. Note that although in h-BX ($X=N, P,$ and As) type stacked bilayer system, the ZBC QVHE can be linked easily to the existence of two physical QVHE, in twisted bilayer graphene it is difficult to obtain such a simplified but physical picture.

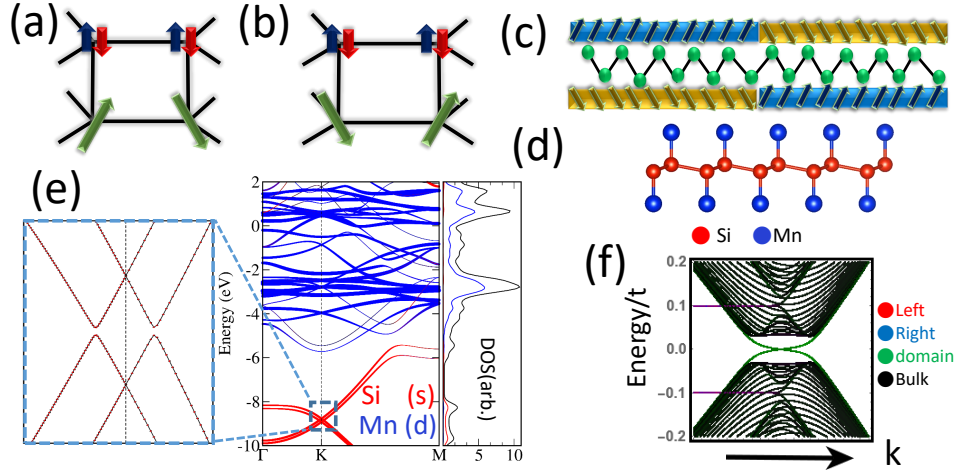


FIG. S3. Realization of the ZBC QVHE in the anti-ferromagnetic and canted anti-ferromagnetic system. Degenerate magnetic moments with canted ground states are shown in (a) and (b). (c) Proximity-induced canted anti-ferromagnetic states in buckled honeycomb layer and domain wall construction by controlling the magnetic proximity. (d) Buckled SiMn monolayer. (e) Band structure of SiMn with canted magnetic ordering for Mn atoms. (f) The energy dispersion of electrons coupled to the canted magnetic domain structure shows ZBC QVHE.

S4. MAGNETIC SYSTEMS

The layer degrees of freedom can be replicated using the spin sector of the magnetic system. The spin configurations in Fig. S3(a,b) produce a similar Hamiltonian as the gapped bilayer AA graphene. However, the layer degree of freedom is replaced by the spin degree of freedom. The canted magnetic configuration (see Fig. S3(a,b)) leads to the following Hamiltonian:

$$H_{\text{magnetic}} = k_x \eta \sigma_x s_0 + k_y \sigma_y s_0 + M^{\text{AFM}} \sigma_z s_z + M^{\text{FM}} \sigma_0 s_x \quad (\text{S.20})$$

where M^{AFM} is the antiferromagnetic part and M^{FM} is the ferromagnetic part (which may arise due to an in-plane magnetic Zeeman field). σ_i , and s_i act on sublattice and spin degree of freedoms. The local symmetry and chiral symmetry are given by $\mathcal{I}_{\text{ST}} = \sigma_x s_x \mathcal{K}$ and $\Pi = \sigma_z s_x$. Here, \mathcal{I}_{ST} is coming as a combination of spin-full time-reversal $\tau = s_y \mathcal{K}(\mathbf{k} \rightarrow -\mathbf{k})$ and $\mathcal{C}_{2z} = \sigma_x s_z(\mathbf{k} \rightarrow -\mathbf{k})$ symmetries. We construct a domain by flipping the sign of the M^{AFM} over the two sides of the domain wall as shown in Fig. S3 (c). The domain have a mirror symmetry $M = \sigma_x(k_y \rightarrow -k_y)$ which interchange domains. Such a domain also respect the domain wall space-time inversion symmetry which is expressed as $\mathcal{I}'_{\text{ST}} = \sigma_x \mathcal{K}$. Two sides of the domain wall possess magnetic configurations similar to Fig. S3 (a) and Fig. S3(b) respectively. For $M^{\text{FM}} = 0$, the system becomes purely anti-ferromagnetic which leads to quantum spin-valley Hall effects. Assuming that the system hosts these two degenerate magnetic solutions, one can naturally expect similar to the Ising model the emergence of magnetic domains due to temporal fluctuations. Furthermore, to achieve a more controllable setup, one can harness desired magnetic states in a buckled honeycomb-like lattice such as silicene by proper magnetic ad-atoms adsorption (Fig. S3(d)) or magnetic proximity effect (Fig. S3(c)). We found that a canted magnetic order on buckled silicene potentially leads to the realization of ZBC QVHE. To confirm such a scenario we artificially construct SiMn lattice structure and assume canted magnetic order on Mn atom (Fig. S3(d)). In Fig. S3(e), we present the band structure of SiMn, where we observe that the d-orbitals of the magnetic Mn atoms, situated around the Fermi energy, induce an effective ZBC QVHE phase for the s-orbitals of silicene well below the Fermi energy (see the magnified view of Fig. S3(e)). Fig. S3(f) confirms the existence of Helical domain states at the interface of two systems with magnetic configurations shown in Fig. S3(a) and Fig. S3(b), respectively.

-
- [1] P. E. Blöchl, Projector augmented-wave method, Phys. Rev. B **50**, 17953 (1994).
 - [2] G. Kresse and J. Hafner, Ab initio molecular dynamics for liquid metals, Phys. Rev. B **47**, 558 (1993).
 - [3] G. Kresse and D. Joubert, From ultrasoft pseudopotentials to the projector augmented-wave method, Phys. Rev. B **59**, 1758 (1999).
 - [4] C. Mondal, R. Ghadimi, and B.-J. Yang, Quantum valley and subvalley hall effect in large-angle twisted bilayer graphene, Phys. Rev. B **108**, L121405 (2023).
 - [5] E. J. Mele, Interlayer coupling in rotationally faulted multilayer graphenes, Journal of Physics D: Applied Physics **45**, 154004 (2012).
 - [6] S. Shallcross, S. Sharma, and O. A. Pankratov, Quantum interference at the twist boundary in graphene, Phys. Rev. Lett. **101**, 056803 (2008).

- [7] M. J. Park, Y. Kim, G. Y. Cho, and S. Lee, Higher-order topological insulator in twisted bilayer graphene, Phys. Rev. Lett. **123**, 216803 (2019).
- [8] E. J. Mele, Commensuration and interlayer coherence in twisted bilayer graphene, Phys. Rev. B **81**, 161405 (2010).
- [9] M. Kindermann, Topological crystalline insulator phase in graphene multilayers, Phys. Rev. Lett. **114**, 226802 (2015).
- [10] B.-B. Liu, X.-T. Zeng, C. Chen, Z. Chen, and X.-L. Sheng, Second-order and real chern topological insulator in twisted bilayer α -graphyne, Phys. Rev. B **106**, 035153 (2022).